Association Aéronautique et Astronautique de France

56th 3AF International Conference on Applied Aerodynamics
28 — 30 March 2022, Toulouse – France

FP92-AERO2022-Gowree

On bio-inspired induced drag reduction techniques

A. Ayvazian, I. Cuenca Alcocel and E. R. Gowree (1)
Dept. of Aerodynamics, Energy and Propulsion, ISAE-SUPAERO, Université de Toulouse, France
(1) *Erwin-ricky.gowree@isae-supaero.fr*

ABSTRACT

The current study was aimed at identifying wing planform geometries which favours low induced drag. The geometries were defined by mathematical functions and following a subsequent parametric study, with a focus on sweep angle and taper ratio, inspired by birds wings and aquatic animals flukes or caudal fins planforms. The parametric studies were carried out using a vortex lattice method (VLM) which was validated with experimental data from literature. The main finding is a confirmation of the fact that the maximum Oswald efficiency factor, ε is not exclusive to an elliptical wing planform. Despite its apparent simplicity, in fact a swept-back-tapered wing with a linear chord distribution can reach $\varepsilon \approx 1$, the limit or minimum induced drag established from elliptical lift distribution. Moreover, the crescent wing geometry, such as the one displayed by the swift, can even surpass this limit.

1. INTRODUCTION

The implementation of new techniques for reducing drag in commercial aircraft will help in reducing fuel consumption and thus emission from aircraft which has detrimental impact on the environment. In the search for new technologies to reduce drag, thanks to its millions of years of evolution based on optimal energy consumption, nature is an exceptional source of inspiration for potential solutions. By taking inspiration from nature here we attempt to identify and propose potential planform geometries for minimum induced drag, seen in migratory birds which display remarkable endurance. The major parameters that defines the planform geometry are the taper and sweep when viewed from the top. Most of the man made systems will consist of a simplified uniform or linear distribution of taper or sweep angle, however when compared to natural flyers, in Fig. 1, the taper, λ and sweep angle Λ are seen to vary in a more non-linear fashion for instance in the crescent-moon shape of the swift's wing, where the from first sight the leading edge can be expected to follow an elliptical profile. In case of the falcon the sweep even changes direction from forward in the inner region to backward in the outer region constituting of the primary feathers, similar variation are also observed on frigates not shown here and is slightly less pronounced on albatross and this configuration will be referred as the "M-configuration" here onwards. In Fig. 1, the corresponding optimised platform geometries emanating from the current study has been presented and interesting point to consider here is that $\lambda \to 0$ in most natural flyers.

The lifting line theory provides a simple model for the induced drag, C_{D_i}, for an arbitrary spanwise lift distribution along the span and it can be expressed as

$$C_{D_i} = \frac{C_L^2}{\pi \varepsilon AR} \tag{1}$$

C_{D_i} is therefore directly proportional to the lift coefficient, C_L^2, and inversely proportional to the aspect ratio AR, and the Oswald efficiency factor, ε which describes how efficiently the lift is distributed along the span, and for an elliptical lift distribution it is equal to 1, thus the minimum induced drag. On a finite wing the spanwise lift distribution is compromised by the spillage at the tip, leading to the formation of tip-vortices which produces the downwash effect leading to an induced drag component and a non-uniform spanwise distribution of circulation. The efficiency of lift generation and the induced drag can be reduced by re-organising the spanwise distribution in lift, through the introduction of taper, twist, sweep, dihedral and local change in aerofoil geometry to quote a few parameters. As a consequence, these parameters were targeted throughout the current study. However, it was demonstrated by Zimmer [12] and later by van Dam [10] that crescent-moon planform shapes inspired

by nature can significantly reduce the induced drag with the Oswald efficiency factor exceed 1, which violates the limit proposed by lifting line theory for elliptical lift distribution.

Amongst the first, van Dam [9] investigated the benefits of the crescent wing geometry inspired by nature. The efficiency of an elliptically-loaded crescent shaped wing was compared with those of an elliptical wing with the same spanwise chord distribution.The crescent wing showed an improvement in the Oswald efficiency factor of nearly 9%. He concluded that the aerodynamic efficiency is improved when the backward curvature was increased. By combining this with a large wingspan, it is possible to greatly reduce induced drag. In this research it was demonstrated also that this type of geometries generated non-planar trailing vortex sheets that produce this important improvement in terms of induced drag. Later BURKETT [1] studied the benefits of aft swept wing tips, similar to that on the swift and the albatross wing. The rearward curvature on these type of wings can reduce the induced drag factor to values below those obtained from unswept elliptical wing once again considered the optimal geometry in classical finite wing theory. These studies showed the potential of crescent wing, like those of swifts, has the possibility to offer significant reductions in induced drag specially at moderate angles of attack. These crescent wings were compared with elliptic geometries during wind tunnel test campaigns at low Reynolds numbers again by van Dam and co-workers [11] [2] confirming the significant reduction in the induced drag, but here the leading-edge separation-induced vortex flow over the highly swept and tapered tips of this type of wings was postulated to be responsible for the benefits.

The current study was intended to revisit the above mentioned induced drag reduction technique and provide further insight into the mechanism which can be exploited for unmanned aerial systems (UAS) and (MAS) applications which operated in similar Reynolds number regime as natural flyers. A low order vortex lattice method (VLM) was first employed to generate the optimal planform geometry tending towards the natural flyers and higher order CFD was then employed to analyse the behaviour of the flow.

2. METHODS

For the geometrical optimisation process the XFLR5 software was used due to its low computational cost, which permits a the simulation and analysis a many cases, of the order of hundreds in this case due to the low order modelling approach. The geometries where obtained by varying the local sweep and taper and this was either done using linear or non-linear functions defined in section 2.1. Once an optimal geometry was identified CFD simulations were conducted using a commercial package to further understand the mechanism of induced drag reduction through the re-organisation of the spanwise flow field.

2.1 Wing planform geometry generation

A major step involved the planform geometry definition based on the bird species. Despite an extensive review of the literature, it was still difficult to obtain the real wing geometry, so we proceeded by analysing images of birds in flight and reconstructed the most representative wing planforms using mathematical functions described below, this allowed for the local change in sweep angle and taper ratio. A series of planform were thus generated using the mathematical functions and was analysed using XFLR5. From equation 1, the induced drag is a strong function of the aspect ratio, AR and C_L, in order to compare the efficiency of different planforms in reducing C_{D_i}, these two parameters had to be kept constant.

2.1.1 Crescent wing

The mathematical functions to define the crescent wing is defined below and also plotted in Fig. 2.2.2 and 2.1.1. Since the elliptical wing planform is known to minimise induced drag, two ellipses were used to define the leading and trailing edges. This helped in defining wing planform similar to that studied experimentally by van Dam [11] shown in Fig. 2.2.2 which also shows the equations and the geometrical parameters used to define this geometry.

Mathematically, an ellipse is defined by the semi-axes, which means that here there are 4 unknowns. In addition to these, an offset for one ellipse has been introduced, in order to have a non-zero wing area in case the leading and trailing edges are the same, like in the case where, $\lambda = 1$ is desired, resulting into 5 unknowns. However, the major axes are considered to be pre-defined parameters, because the wingspan, b, is kept constant throughout the entire study, thus reducing the system of equations to 3 unknowns. Since the, taper ratio, λ is known to affect the spanwise loading and thus induced drag it was kept as a variable. To achieve a crescent wing planform sweep, α, was introduced which connected the leading edge at the tip and the root would also impact the planform shape of the wing and therefore the induced drag. The parameters y_1 and y_2 are not related to the wing planform, they instead represent the semi-minor axes of the ellipses. h represents the chord length at the tip and is directly linked to the offset of the equation representing the leading edge. After some mathematical manipulations, the resulting constraints are expressed in Eqs. 2, 3 and 4 below.

$$y_1 = \frac{1}{2} b sin(\alpha) \tag{2}$$

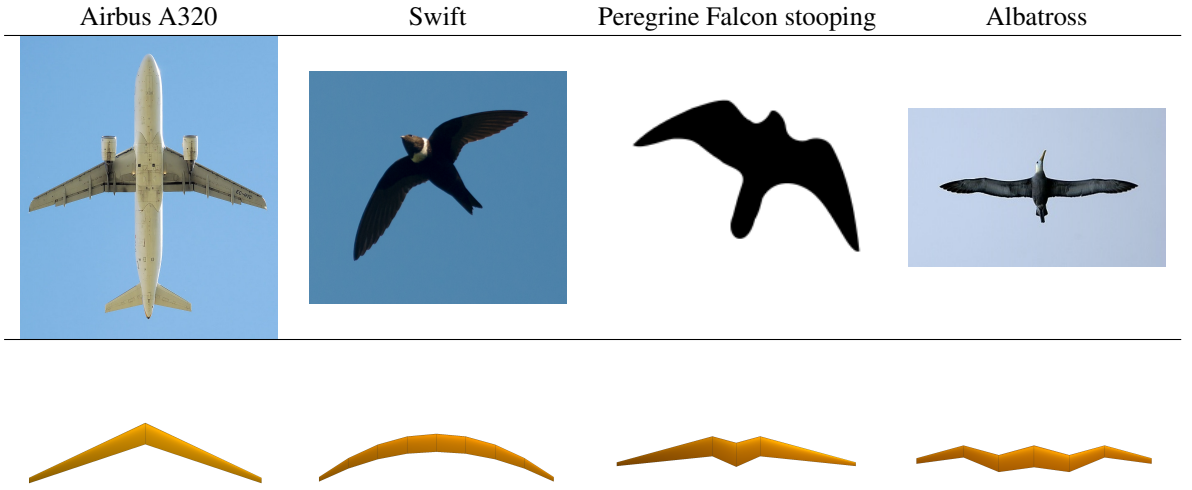

Table 1: Illustration of some wing planforms observed in nature and from man-made systems. Images from open access sources.

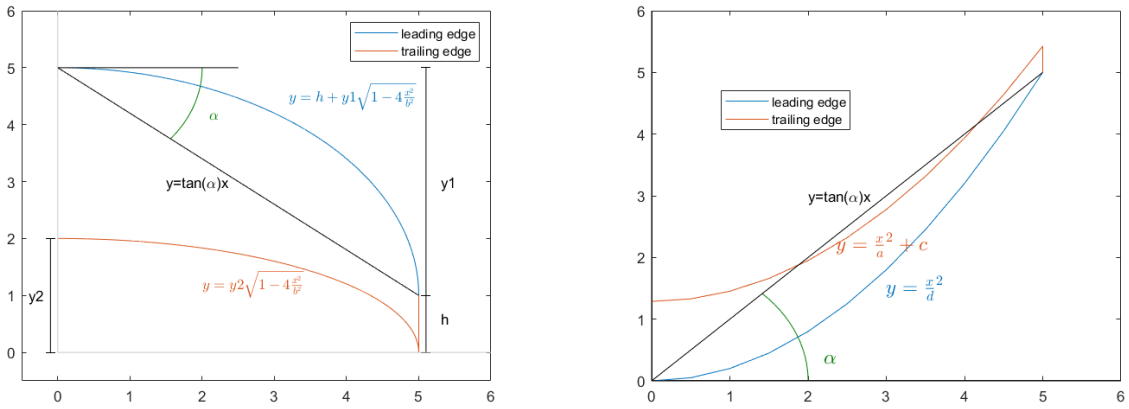

Figure 1: The leading and trailing edge functions to define the geometry of the elliptical crescent wing on the left and the parabolic crescent wing on the right

$$h = \frac{b}{AR(1-(\lambda-1)\frac{\pi}{4})} \tag{3}$$

$$y_2 = y1 + (\lambda-1)h \tag{4}$$

In this study we also studied crescent wings defined by parabolic functions, which can be defined by the functions shown in Figure 2.1.1. Again, there are three constants that need to be determined in order to define the wing planform: a, c and d. The parameters chosen to act as constraints are the same as in the case of the crescent wing defined with elliptical functions: λ, AR and α. The wingspan, b, is kept constant throughout all the studies, therefore it was treated as a known parameter. Following some mathematical manipulations, the constraints imposed could be expressed, equations Eqs. 5, 6 and 7.

$$d = \sqrt{\frac{0.5b}{tan(\alpha)}} \tag{5}$$

$$a = \sqrt{\frac{AR\phi(d^2)}{4d^2 + bAR\phi}} \tag{6}$$

$$c = (\frac{1}{a^2} - \frac{1}{d^2})\frac{b^2}{4(\lambda - 1)} \tag{7}$$

where ϕ is a parameter introduced for mathematical convenience:

$$\phi = \frac{1}{3} + \frac{1}{\lambda - 1} \tag{8}$$

2.1.2 M-configuration wing

The albatross is also a high endurance flyer [8], but their wing planform as shown on the top of Fig. 2 is very different to the crescent wing. Unlike in the case of the crescent wing the planform geometry is defined as a linear variation of the sweep and taper, as shown at the bottom of Fig 2, in this case both a backward and a forward sweep was required. The parameters $s1$ and $s2$ represent the positions where the sweep angle $\alpha 1$, $\alpha 2$ and $\alpha 3$ are defined, but $\alpha 1$ and $\alpha 3$ were always kept over 270° during the study, so they were effectively backward sweep angles. The parameters imposed on the M wing geometry were the sweep and the taper ratio, a linear chord distribution along the wingspan. These yielded constraints on the root chord length (c_{root}), the tip chord length (c_{tip}) and the slope of the linear function defining the chord distribution along the wingspan (c_{slope}) given by equation 9, 10 and 11

$$c_{root} = \frac{2b}{AR(1 + \lambda)} \tag{9}$$

$$c_{tip} = \lambda c_{root} \tag{10}$$

$$c_{slope} = \frac{2(c_{tip} - c_{root})}{b} \tag{11}$$

2.2 Numerical methods

CFD simulations were also conducted, for seeing the behaviour of the flow around the shape of crescent wings. For validating the CFD methods used, the wing geometry of [11] experimental studies, Figure **??**, was simulated with STAR-CCM+. The models used

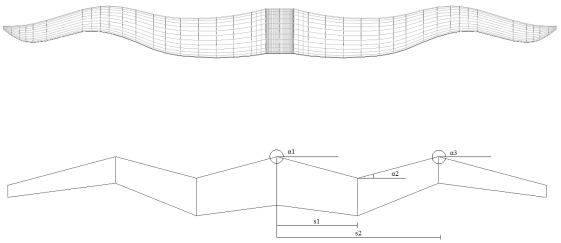

Figure 2: The parameters used to define the M wing geometry.

for the simulation were $K - \omega$ turbulence model with the submodel turbulence supression for simulating the boundary layer transition at the 5% of the chord. The computational domain used was defined by 20 chords downstream, 5 chords upstream and 7 chords for top and bot margins. A mesh independence study was carried on resulting finally in a mesh of around 5.300.000 cells.

2.2.1 Low order modelling

2.2.2 High order modelling

Following the optimisation using XFLR5, more detailed RANS simulations were undertaken to generate further insight into the behaviour of the flow, limited in XFLR5, we would like to emphasis on the fact this approach was not used to calculate the induced drag directly. Here, the commercial package STAR-CCM+ was employed. The computational domain was defined by 20 chords downstream, 5 chords upstream and 7 chords for top and the bottom of the wing placed at the centre. In order to resolve the flow in the wake downstream a cubic region of very fine mesh was introduced as shown in Fig. at least part of the evolution of the vortical flow downstream. For very accurate calculations of the induced drag from the quantities in the wake, such a mesh needs to be extended until the Treftz plane which can be assumed to start at approximately 50 chords downstream at least which would result in a very large number of cell. Calculations with such as number of cell was not feasible within the scope of this project, but as shown in section 2.3, the RANS simulation was reliable enough to provide the spanwise loading and the total lift which could in agreement with experimental data of van Dam and co-workers [11]. The $k - \omega$ turbulence model with a turbulence supression submodel for simulating the boundary layer transition at 5% chord was employed so as to simulate the tripping position during the experiment. A mesh independence study was carried-out on the unstructured mesh resulting in a total number of mesh of around 5.3 million cell showing the best compromise.

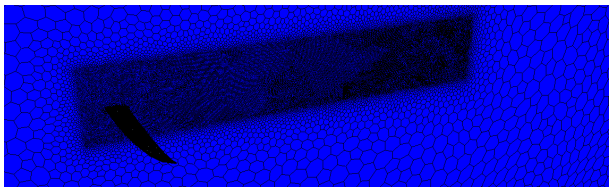

Figure 3: The mesh refinement in the wake of the wing

2.3 Validation of numerical methods

Although, XFLR5 has shown to be very reliable for 2D aerofoils over a large range of Reynolds number, the 3D calculation over finite wings has not received a thorough validation in the literature. In addition, due to the highly dissipative characteristics of unstructured RANS simulation which also handles the flow in the far wake rather poorly, due to the expansion in the cell size downstream for a better compromise in terms of simulation time and cost. Here, we proceeded by a verification of the numerical method with the experimental results of van Dam and co-workers [11] in the subsonic wind tunnel at NASA Langley. The experiment was conducted over a crescent wing shown on the top left of Fig. 4, with an $AR = 6.9$ at a Reynolds number $Re = 4.8 \times 10^5$ based on the root chord and Mach number, $M = 0.205$ for a range of angle of incidence. A similar geometry and flow conditions were simulated in XFLR5 using both the LLT and VLM methods with transition fixed at 5% chord during the 2D batch calculations. In RANS formulation the $K-\omega$ turbulence model and the turbulence surpression sub-model was employed for simulating the boundary layer transition at 5% of chord as in the experiment.

From the total lift coefficient, C_L shown on the top right of Fig. 2.3, an expected linear variation due to the Reynolds number being sufficiently high and in the presence of a boundary layer trip is observed. While the results from LLT methods showed noticeable over-prediction with respect to the experimental results, the VLM methods showed closer agreement. No, noticeable difference was found between the number of panels and therefore the rest of the optimisation process using XFLR later was undertaken for 2000 panels. The RANS results also showed acceptable agreement while being slightly under-predicted. The total drag coefficient, C_D showed the usual U-shape behaviour where drag increases with increasing angle of attack. At zero lift the total drag constitute purely of the profile drag which can be split into skin friction drag and form drag. But, with increasing angle of incidence the contribution of form drag and now induced drag starts to increase and cannot be easily separated from the total drag. Once again the VLM method showed reasonable agreement with respect to the experimental results, while the LLT was significantly under-predicting the drag. Except at zero or very low angle of attack or lift condition, the results from the RANS simulation was significantly over-predicted. This is due to the inability of RANS to account for the increase in form drag, but more importantly the induced drag as the quantifies in the far wake suffers from dissipation potentially due to the meshing strategy, resulting in large errors in calculating the total drag, from integration of the far wake quantities.

When comparing the spanwise lift distribution on the bottom right of figure Fig. 2.3 and elliptical C_L distribution is observed, where the agreement between the experiment, VLM method and the RANS simulations are satisfactory up to about a 80% along the span. Further outboard the numerical simulation results showed slightly better agreement as opposed to the VLM method. From this comparison, it is fair to suggest that he RANS simulation can predict the near-field with reasonable accuracy and could be therefore employed to study the spanwise re-arrangement in the flow field over the wing to generate further insight into the potential induced drag reduction mechanism, despite the overall induced drag prediction being unreliable due to the meshing strategy. Since, the current validation was undertaken over a crescent wing the analysis that follows could be carried-out with reasonable fidelity.

3. PARAMETRIC STUDIES

For all the parametric optimisation studies, in order to have comparable geometries, the Aspect Ratio was kept constant at 17.664. This is in the range of the average values of the adults albatross [7], and they were chosen because they are representative of animals and UAV geometries. The airspeed was selected to 20 m/s, which is the normal cruise speed of the albatross corresponding to an average $Re \approx 250 \times 10^3$

3.1 Tapered Wing

From the literature the two influential geometric parameters for induced drag were identified as the taper taper ratio and the sweep. In conventional subsonic, transonic or supersonic wing design, the later is usually favoured for the reduction of wave drag or increase in drag divergence Mach number and improvement of stability but little consideration has been given for induced drag. Here, we revisited the effect of uniform sweep and taper on induced drag starting from a rectangular planform. Following the parametric optimisation process, from the top Fig. 5, even for a simple uniform sweep and taper the Oswald efficiency factor can be increased to a value of 1 (shown by the red dot), which corresponds to the minimum achievable from lifting line theory based on an elliptic lift or circulation distribution. This is achieved for

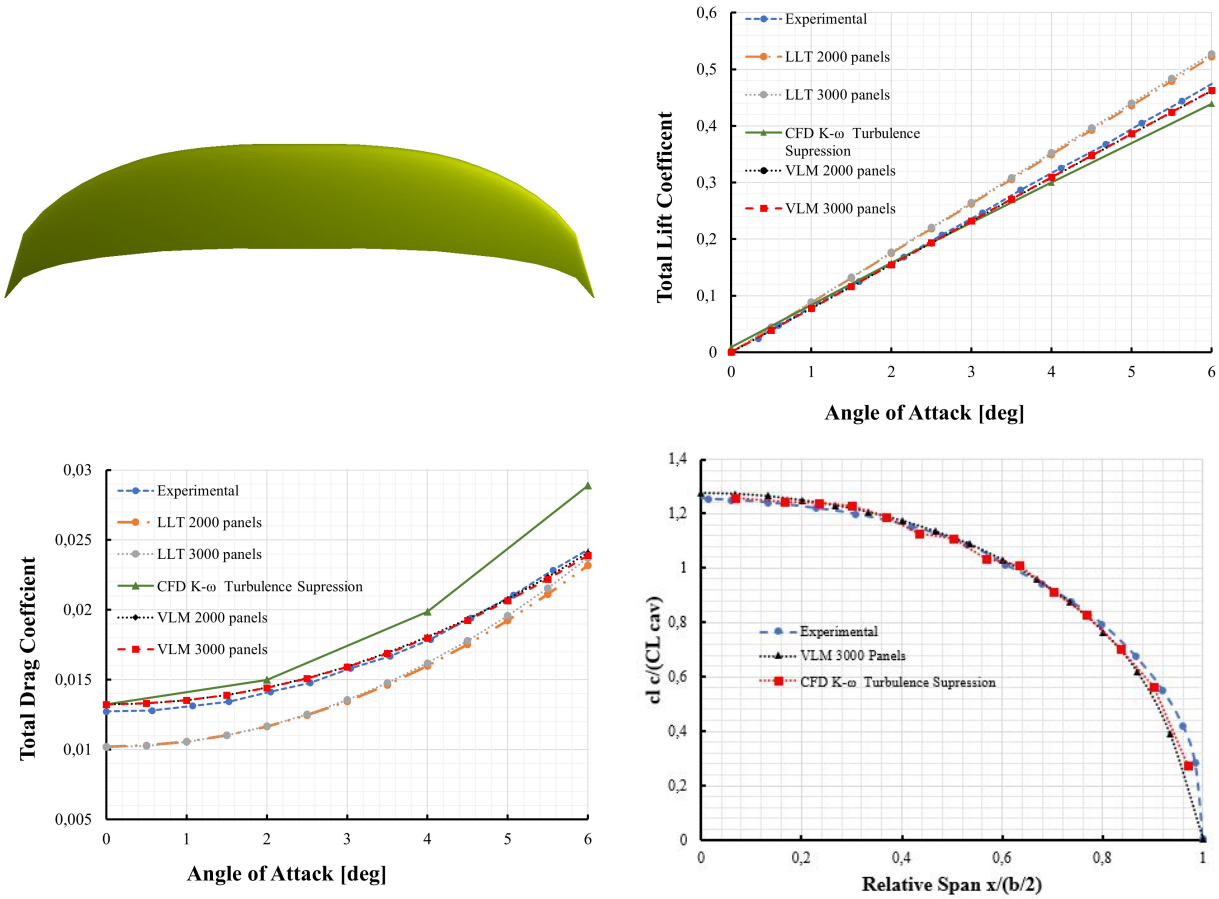

Figure 4: The top left shows the crescent wing tested experimentally by van Dam [11]. The top right and bottom left shows the total lift and total drag coefficient from the experiment, LLT, VLM and CFD calculations. Bottom right, spanwise distribution of lift from the experiment of van Dam and from the VLM and CFD calculations.

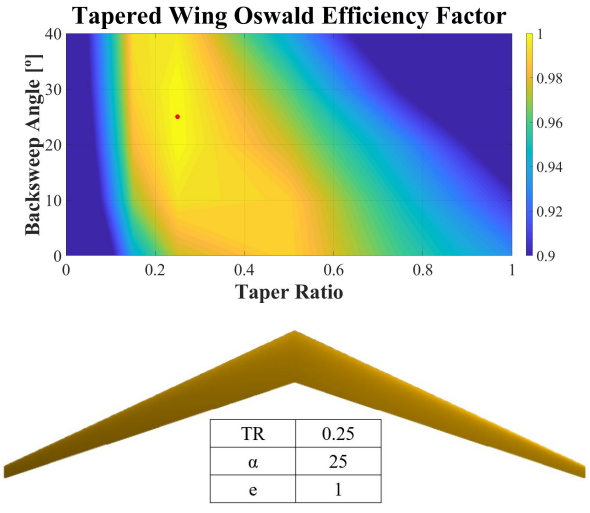

Figure 5: Effect of sweep angle and taper ratio on the Oswald efficiency factor, ε, on the crescent wing with parabolic (middle) and elliptic (bottom) wing planform profile.

the case of $\lambda = 0.25$ and sweep angle of 25°. The current finding has not been reported previously on uniform swept-tapered wing, however most of the previous studies have been focussed on high Reynolds number and taper ratio. The effect of low freestream Reynolds number which reduces even further the local Reynolds number towards the tip can affect the local lift and this has not been exploited to great length.

3.2 M-configuration

Following on with uniform sweep and taper configurations, the effect of changing the direction of the sweep angle in the in-board section of the wing can be implemented through the M-configuration defined above. This configuration is expected to approach the planform geometries of albatross, also known for very high endurance. A similar optimisation process to that in the section above was adopted and in this case 5 parameters can be varied, the back or forward sweep angles, α_1, α_2 and α_3, and two breakpoint position along the wingspan where these angles were varied, S_1 and S_2. In order, to

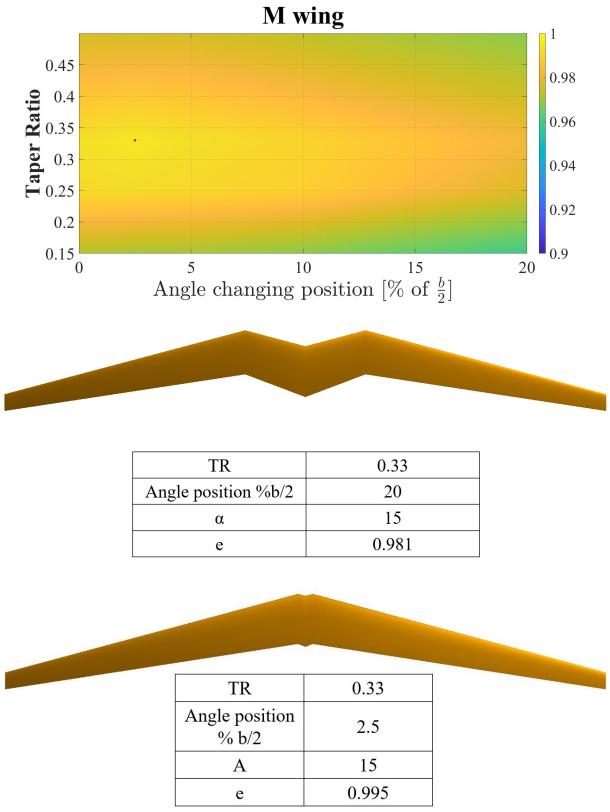

TR	0.33
Angle position %b/2	20
α	15
e	0.981

TR	0.33
Angle position % b/2	2.5
A	15
e	0.995

Figure 6: Effect of sweep angle and taper ratio on the Oswald efficiency factor, ε on the M-configuration

reduce the number of variables in the absence of an optimiser, it was decided to assume the angles α share the same absolute value and all of them are changed together rather than independently, the breakpoint positions where the uniform sweep and taper is applied $s1$ and $s2$ shown in 2 have been linked by imposing $s2 = 2 \cdot s1$.

Following the optimisation process, it was rather surprising to see that the M-configuration which was qualitatively representative of the albatross wing did not yield a high Oswald efficiency factor, in fact it was well below the optimised uniform swept-back-tapered configuration shown in Fig. 5, with $\varepsilon = 0.981$. The efficiency factor of such configuration could be further improved by starting the breakpoint position, where the second aft sweep is applied, α_3, further inboard as shown in the contour plots in Fig.6. This resulted in a planform tending towards the uniform swept wing in Fig. 5 and for the case of breakpoint position at 2.5% of span as shown at the bottom of Fig. 6 the Oswald efficiency factor tended towards a value of 1.

3.3 Crescent Wing

The crescent wing can be considered as a swept-tapered wing with a non-linear spanwise profile of the leading and trailing edge. Using the same optimisation process as earlier, from the top of Fig. 7 the effect of varying the sweep angle as a function of taper is shown for the planform with a parabolic and elliptic profile. The region where the Oswald efficiency factor $\varepsilon > 0.95$ expanded over a larger portion of the sweep and taper map as opposed to the uniform swept-tapered and non-uniform swept-tapered M-configuration. In fact both types of crescent wings could easily achieve Oswald efficiency factor, $\varepsilon \geq 1$, for sweep angle of 10°, where the parabolic planform attained a maximum of $\varepsilon = 1.005$ for a taper ratio, $\lambda = 0.25$ and the elliptic planform was marginally higher with, $\varepsilon = 1.008$, for a much smaller taper ratio, $\lambda = 0.1$.

For both parabolic and elliptic planforms, the sweep angle of 10° quoted here is only applicable very close to the root of the wing as it was introduced in a way to vary the local change in curvature. However, this leads to a local change in sweep angle which can increase very rapidly along the span of the wing, whereby exceeding values of 60° in the out-board region of the elliptic planform. On the other hand, for the elliptic wing the very low taper ratio would result in relatively low Reynolds number in the outboard region and would be prone to laminar separation. The viscous-coupled VLM method in XFLR5 could potentially account for the local change in Reynolds number, since the 2D viscous calculation from XFLR5 has been demonstrated to deal with low Reynolds number cases quite reliably. However, three-dimensionality in the viscous flow due to large change in local sweep angle and the formation of large cross-flow components cannot be modelled with the 2D approach of XFLR5. The combination of high sweep and low Reynolds number towards the tip would favour the formation of leading edge vortices which would generate extra lift due to the contribution from vortex lift. This prompted further studies of the flow field over the wing.

4. THE SPANWISE FLOW FIELD OVER THE WING

During the optimisation exercise in the previous section only the overall performance of the wing was characterised using the VLM method in XFLR5. It was demonstrated that if the sweep and taper is varied optimally the minimum induced drag condition, $\varepsilon = 1.0$, predicted from lifting line theory can be achieved or even surpassed. From the spanwise evolution of the local lift normalised by the total lift presented in Fig.8, a major difference can be observed between the rectangular planform, which shows the traditional elliptical lift distribution and the rest of the configurations emanating from the current optimisation study. The swept-tapered and the M-configuration showed similar trend in spanwise loading with low inboard loading and higher out-board loading compared to the rectangular case, as seen on conven-

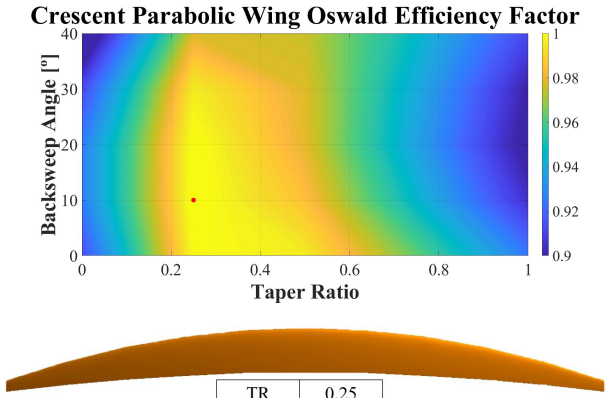

TR	0.25
α	10
e	1.005

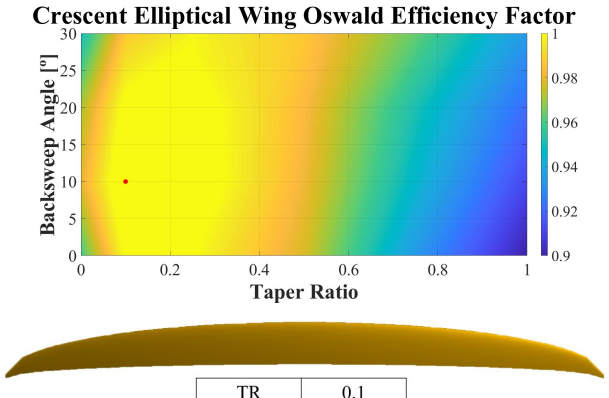

TR	0.1
α	10
e	1.008

Figure 7: The results of the optimisation process for the crescent with a parabolic and elliptical planform profile on the left and right respectively. The figures at the bottom shown the optimal geometry.

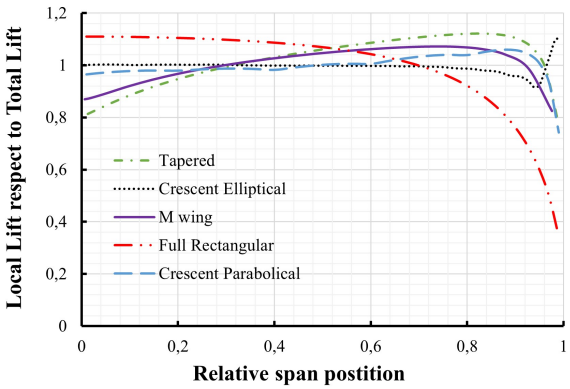

Figure 8: Spanwise lift distribution of the main geometries studied at AoA=6^o with VLM

tional swept-tapered transonic wing. However, from Tab 2, the conventional swept-tapered civil aircraft achieves an Oswald efficiency factor lower than the optimal swept-tapered wing defined here which could attain a value of 1. However, the spanwise loading from the crescent wing showed a more intriguing characteristics, for the case of the parabolic planform very small or almost negligible variation in the lift was observed starting from the inboard region up to almost 60% along the span, where it increased and started dropping at approximately 95% of span with a trend similar to the swept-tapered wing. On the other hand the crescent wing with elliptic planform experienced larger extent of the constant spanwise lift, upto to 80% and unlike the parabolic planform underwent a marginal reduction upto around 95% of span where it increased rapidly again. This behaviour was predicted by the viscous-VLM method which is in fact a representation of the 2D viscous flow calculated from XFLR5 as a function of Reynolds number which reduces along the span in this case.

Along the elliptic crescent wing the sectional Reynolds number, Re, ranged from 290×10^3 at the root to 29×10^3 at the tip, for $Re < 100 \times 10^3$ a large laminar separation bubble was predicted from the 2D XFLR5 viscous calculation at an incidence of 6° and therefore in the presence a high local sweep the strong spanwise velocity component would generate a vortex which would contribute to the additional lift. In order, to support this hypothesis further RANS simulation was conducted on the elliptic crescent wing and a rectangular wing with similar aspect ratio for comparison. Even if the overall drag prediction was not in agreement with the experimental results, here we were only interested in the flow over the near-field of the wing and from the bottom right of Fig.4 the spanwise loading from the RANS simulations is seen to predicted with a reasonable accuracy when compared with the experimental results. Therefore, we proceeded with RANS simulation with a mesh of approximately 13 millions cells on a rectangular wing and the optimal elliptic crescent wing. In this case the γ transition model was used in addition to the $k-\omega$ turbulence model. The topology of the flow over these two configurations is presented in terms of Q-criterion iso-surfaces coloured by vorticity in Fig. 9, from these two configuration the tip vortices are clearly put into evidence, however the most noticeable differences is in the region right before the tip where an additional pair of vortices can be observed in the case of the elliptic planform. The presence of this pair of vortices are clearer when comparing a plane orthogonal to the streamwise flow immediately downstrea the trailing edge in Fig. **??**. This is further evidence of the presence of the vortex lift prevailing from the vortical struture similar to a leading vortex postulated earlier.

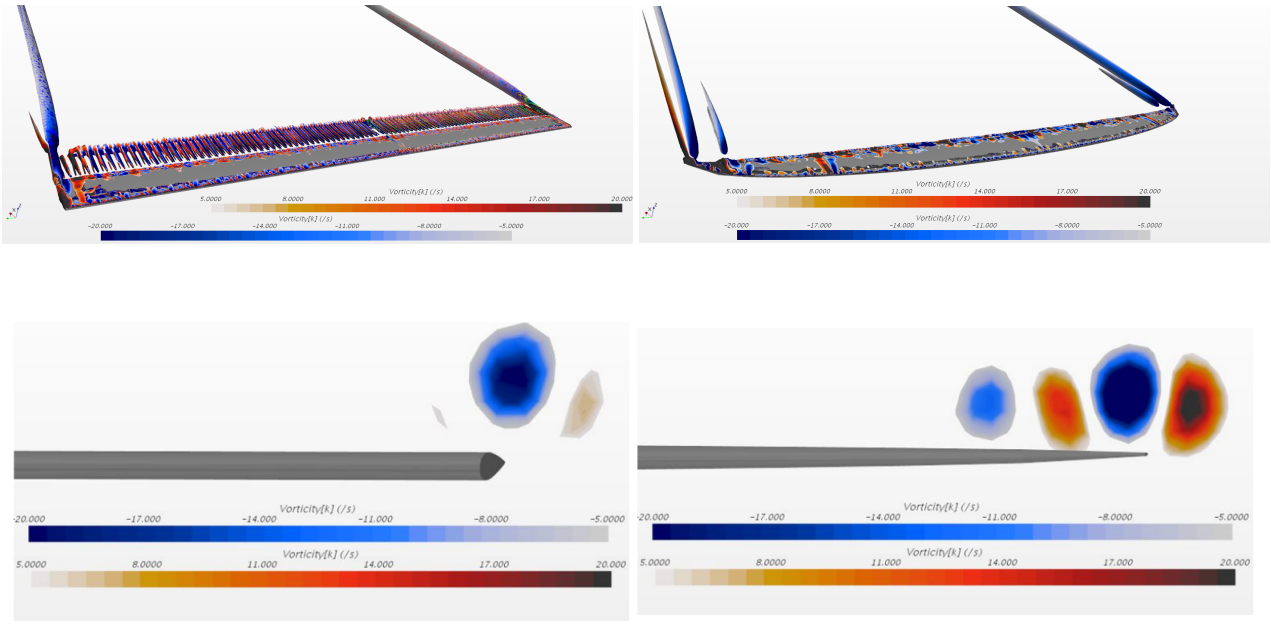

Figure 9: Q-criterion iso-surface coloured by vorticity over rectangular wing on the left and elliptic crescent wing on the right.

Aircraft/wing	e	Cl
A320	0.922	0.52
A388	0.927	0.40
B737	0.921	0.62
B748	0.924	0.44
CP Van Damn Experimental	1	< 0.5
Optimum tapered wing	1	0.63
Albatross wing geometry	0.973	0.63
M wing	0.995	0.63
Crescent (parab.)	1.005	0.63
Crescent (ellipt.)	1.008	0.63

Table 2: Geometrical characteristics and efficiency of the optimized elliptical functions based crescent wing. Aircraft's data taken from [6]

5. CONCLUSION

Here we have demonstrated that the VLM method in XFRL5 can provide a reliable estimate of the spanwise loading and thus induced drag when compared with existing experimental results in the literature. This was an important step towards validating the low-order modelling which was then employed to optimise wing planform geometry with lower induced drag characteristics. From a simple uniform variation of sweep and taper we showed that an Oswald efficiency factor of 1 which defines the minimum induced drag from lifting line theory can be attained. The efficiency factor could be further increased for the variation in sweep and taper applied in a non-linear fashion to approach planform geometries found in nature. Here the crescent moon shape observed on the wings of swifts and swallows and, the caudal fins and flukes in thunniforms and caetaceans, achieved the highest efficiency factor when fitted with an elliptic leading and trailing edge chord distribution, inspired from existing knowledge of the benefit from the elliptic loading. Preliminary CFD simulations have shown that in addition to the tip vortices, for the crescent wing a combination of low Reynolds number and high sweep towards the tip favours the formation of another vortex which provides additional loading towards the tip and thus improving the efficiency of the overall wing in producing lift and thus reducing the induced drag.

REFERENCES

[1] C. W. BURKETT. Reductions in induced drag by the use of aft swept wing tips. *Aeronautical Journal*, 1:400–405, 1989.

[2] C. P. van Dam, P. M. H. W. Vijgen, and B. J. Holmes. Aerodynamic characteristics of crescent and elliptic wings at high angles of attack. *Journal of Aircraft*, 28:253–260, 1991.

[3] E. R. Gowree, C. Jagadeesh, E. Talboys, C. Lagemann, and C. Brucker. Vortices enable the complex aerobatics of peregrine falcons. *Communications Biology*, 1-27, 2018.

[4] I. Kroo. Drag due to lift: Concepts for prediction and reduction. *Annual Review of Fluid Mechanics*, 1:587–617, 2001.

[5] M. M. Munk. The minimum induced drag of aerofoils. *NACARept. 121,*, 1, 1923.

[6] M. Nita and D. Scholz. Estimating the oswald factor from basic aircraft geometrical parameters. *Deutscher Luft- und Raumfahrtkongress*, 2012.

[7] P. L. Richardson. How do albatrosses fly around the world without flapping their wings? *Progress in Oceanography*, 88:46–58, 2011.

[8] A. Stempeck, M. Hassanalian, and A. Abdelkefi. Aerodynamic performance of albatross-inspired wing shape for marine unmanned air vehicles. *Aviation Technology, Integration, and Operations Conference*, 2018.

[9] C. P. van Dam. Efficiency characteristics of crescent-shaped wings and caudal fins. *Nature*, 325:435–437, 1986.

[10] C. P. van Dam. Induced-drag characteristics of crescent-moon-shaped wings. *Journal of Aircraft*, 2:115–119, 1987.

[11] C. P. van Dam, P. M. H. W. Vijgen, and B. J. Holmes. Experimental investigation on the effect of crescent planform on lift and drag. *Journal of Aircraft*, 28:713–720, 1991.

[12] H. Zimmer. The significance of wing end configuration in airfoil design for civil aviation aircraft,. *NASA TM-75711*, 1, 1979.